Available online at www.sciencedirect.com
SCIENCE DIRECT®
Journal of Nuclear Materials 353 (2006) 135–145
journal of nuclear materials
www.elsevier.com/locate/jnucmat

Effects of tube fabrication variables on the oxidation of experimental Zr–2.5Nb tubes

C. Nam [a,*], J. Lin [a], H. Li [a], J.A. Szpunar [a], R. Holt [b]

[a] *Mining, Metals and Materials Engineering, McGill University, Montreal, Que., Canada H3A 2B2*
[b] *Mechanical and Materials Engineering, Queen's University, Kingston, Canada*

Received 15 September 2005; accepted 3 February 2006

Abstract

Experimental Zr–2.5Nb tubes, manufactured with various fabrication routes, were oxidized in air at 400 and 500 °C, and their oxide–metal interfaces are characterized by scanning electron microscopy. Various tube microstructures are formed depending to a large extent on the extrusion temperatures in the range of 650–975 °C. The second phase distribution of the tube has a great impact on the oxidation resistance. The tubes that have fine and discrete second phase structures show a superior oxidation resistance to those of coarse and continuous second phase structures. The oxide interface structure evolves as the oxide grows by mirroring the metal microstructure at the beginning of the oxidation, and then develops either a rough structure at higher oxidation rate or a flat structure at lower oxidation rate. The oxide granules in the flat interfaces grow with increases both in oxide thickness and oxidation temperature, but the granule size is held constant in the rough interfaces. Therefore, the oxidation resistance of Zr–2.5Nb tube may be improved when the tube has fine distribution of second phases with the formation of a flat structure at the metal–oxide interface.

PACS: 81.65.Mq

1. Introduction

In CANDU nuclear reactors, pressure tubes made of Zr–2.5wt%Nb alloy are used to contain uranium fuels and the water coolant. Hydrogen accumulations in the pressure tube as a result of the corrosion reaction between the zirconium tube and the water coolant can form hydrides that may limit the lifetime of the pressure tube in the reactor core. Since the oxide film on the tube surface acts as a barrier against hydrogen permeation and further oxidation, the integrity of the pressure tube is critically dependent on the protectiveness of this oxide barrier. The oxide formed on zirconium-based alloys usually consists of two layers, a dense and protective inner layer and a porous and non-protective outer layer. Therefore, the oxidation rate is mainly controlled by the inner layer of the oxide near the oxide–metal interface.

To better understand the oxidation mechanism, the structure of the oxide–metal interface has been analyzed by scanning electron microscopy (SEM). The great depth of field in the SEM allows one to observe topographic characteristics of the

* Corresponding author.
E-mail address: cheol.nam@mcgill.ca (C. Nam).

0022-3115/$ - see front matter © 2006 Elsevier B.V. All rights reserved.
doi:10.1016/j.jnucmat.2006.02.091

oxide–metal interface. For the SEM analysis of the oxide–metal interface in Zr alloys, the metal substrate is often dissolved in a chemical solution. These interface observations have revealed that the oxide interface structure changes as the oxide thickens. In the Zircaloys, the oxide interface in the pre-transition region of oxidation has a fine granular structure, whereas a cauliflower structure is typically observed in the post-transition region [1–5]. Unlike the Zircaloys, the Zr–2.5Nb tube has a two-phase structure of ($\alpha + \beta$), which has a great influence on the development of the interface structure during oxidation. At the interface of the Zr–2.5Nb, oxide ridges formed at areas where β-Zr phase was consumed by the oxide [4–7]. As the oxide grew, the protruding ridges became wider and deeper, and started to coalesce in different zones of the interface [5]. These observations on the Zr–2.5Nb have been made only for the oxide grown on standard pressure tubes.

There have been no reports of corrosion resistance and the interface structure depending on fabrication variables particularly extrusion temperature of Zr–2.5Nb tubes. These days, the standard Zr–2.5Nb pressure tube is fabricated by hot extrusion at about 815 °C after β-quenching in billet preparation. As a final fabrication step, the tube is autoclaved for 24 h in 400 °C steam to form a protective oxide film and to relieve residual stresses. Previous work has shown that the extrusion temperature has a remarkable effect on the formation of texture and microstructure [8,9] as well as on the mechanical properties [10] of Zr–2.5Nb tubes. No such results have been documented on the corrosion resistance with the extrusion temperature. Different fabrication route of the tube leads to different tube microstructure mainly in terms of grain size and β-phase distribution. A computer simulation showed that substrate grain size and β-phase distribution contribute the oxidation rate of the Zr–2.5Nb tube [11].

The interface morphology may be correlated with oxidation resistance of Zr–2.5Nb alloys. Differences in substrate microstructure generated by different processes can be responsible for differences in the interface morphology. In the present work, the experimental Zr–2.5Nb tubes have been manufactured by applying various fabrication routes at the billet and extrusion stages and had a wide range of tube microstructures. These tubes were oxidized in air, and the oxide–metal interfaces are characterized at several oxide thicknesses. The relationships between the tube microstructure, oxidation resistance and the interface structure are presented as well.

In this work, oxidation tests were conducted in atmospheric air environment which is much different from in-reactor condition of CANDU reactor where high pressure heavy water is circulating under high flux neutron environment. In this regard, the present results cannot represent expected oxidation behavior in CANDU. Nonetheless, large similarities of zirconium oxidation behavior were observed between in water and in air oxidation, for their oxide structure [12–14], oxidation kinetics [15,16], oxide texture [17] and influence of annealing on oxidation rate [18,19]. Therefore, present results obtained in air may give some insight into optimization of tube processing and oxide–metal interface evolution in pressure tubes for CANDU reactor application.

2. Experimental

2.1. Materials

A set of 'micro-pressure-tubes' made of Zr–2.5wt%Nb were manufactured by NU-TECH Precision Metals Inc. in Canada, through six different routes as shown in Fig. 1 and Table 1. All tubes were made from the same ingot. The manufacturing variables were billet cooling (β-quenched or β-slow-cooled) and hot extrusion temperature (650, 815 or 975 °C). They were all cold-drawn 27% and autoclaved at 400 °C for 24 h, and these are as-received tubes. All specimens were taken from the front ends of the tubes, which were the ends that emerged first in the extrusion press. Some tubes were subsequently annealed at 580 °C for 100 h in a laboratory furnace. Compared with standard pressure tubes, these experimental tubes have a much reduced size with a wall thickness of 3 mm and an inside diameter of 9 mm.

2.2. Oxidation test and X-ray diffraction

The oxidation tests were performed at either 400 or 500 °C in air environment. The 400 °C oxidation test was conducted in a furnace up to 50 days without removing as-received oxides. Prior to the 500 °C oxidation test, the inside of tube was machined out and thinned to a wall thickness of 1 mm to oxidize mostly on circumferential-axial surfaces of the tube for oxidation tests. Then the remaining outside

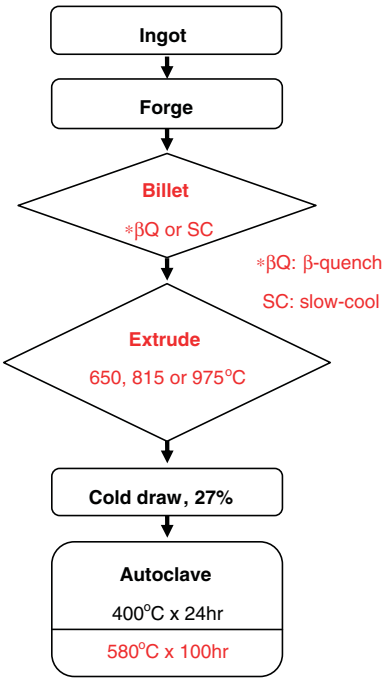

Fig. 1. Fabrication processes of the Zr–2.5Nb experimental tubes.

Table 1
Fabrication variables of the experimental Zr–2.5Nb tubes

Tube ID	Billet cooling[a]	Extrusion temperature (°C)	Extrusion ratio
62	β-Q	650	4:1
63	β-Q	815	10:1
64	β-Q	975	10:1
65	SC	650	4:1
66	SC	815	10:1
67	SC	975	10:1

[a] β-Q and SC (slow-cooling) were performed in water and furnace, respectively.

oxide was removed by grinding, and the tube samples were pickled in $30H_2SO_4 + 30HNO_3 + 30H_2O + 10HF$ solution for about 1 min. These samples were then oxidized for three days in flowing air using a thermogravimetric analysis (TGA).

The X-ray diffraction measurements were done for second phase identification in the radial-axial plane of the tubes. A Rigaku DMax-500 X-ray diffractometer was used with Cu K_α radiation at 40 kV and 120 mA. Acquisition time was set at 10 s with 0.03° step interval at the 2θ range of 20–80°.

2.3. Characterization of the interface structure

To observe on the same picture of both the oxide interface and metal substrate, a sample preparation procedure has been devised for SEM micrographs, as shown in Fig. 2. The first step was mounting a tube specimen after cutting the oxidized tube with a slow speed diamond saw. Then the mounted specimen was ground until the oxide and metal areas were in the same plane. The last step was chemical etching with a solution of $45HNO_3 + 45H_2O + 10HF$ by a swabbing method. To reduce charging in the SEM observation, samples were coated with around 30 nm thickness of gold/palladium layer by sputtering. All the SEM examinations were performed using a Philips XL30 FEG-SEM.

3. Results

3.1. Second phases in experimental Zr–2.5Nb tubes

Fig. 3(a) shows X-ray diffraction patterns for second phases of the as-received tubes. The second phase peaks of hcp ω $(20\bar{2}1)$ and bcc β (200) were seen at all the tubes except the tube 62 where only the β (200) peak was observed. Content of Nb in

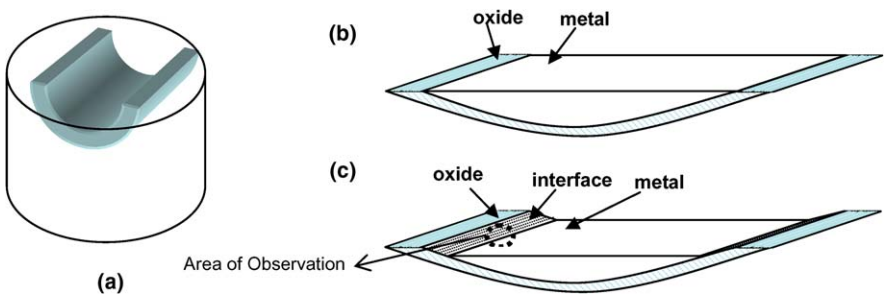

Fig. 2. Schematic diagram showing sample preparation procedure for SEM micrograph of the oxide–metal interface: (a) mounting of tube sample, (b) mechanical polishing, and (c) chemical etching.

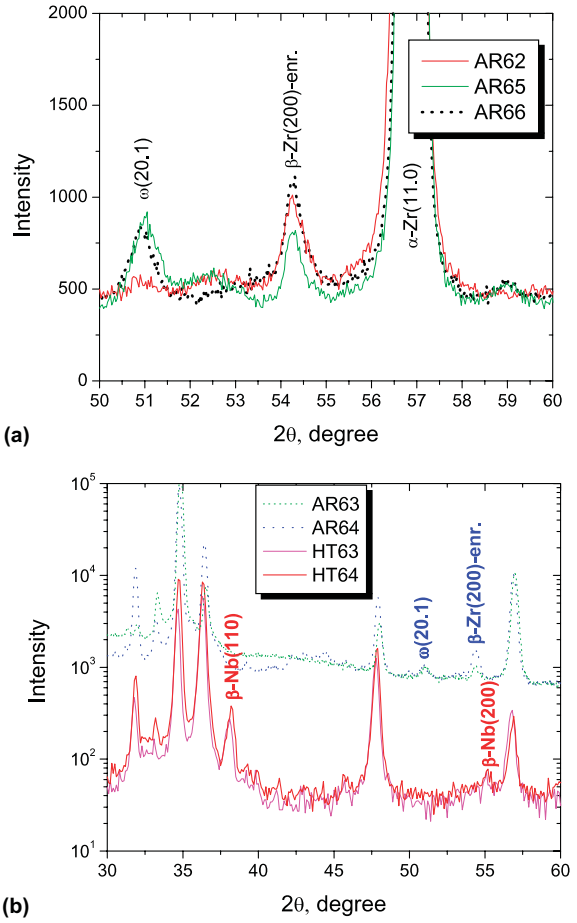

Fig. 3. X-ray diffraction patterns of the Zr–2.5Nb tubes showing (a) second phases (ω and β) of as-received tubes, and (b) transformation of the second phases upon heat treatment; AR and HT stand for as-received and heat-treated (580 °C for 100 h) tubes, respectively.

the β-phase can be determined thanks to the fact that Vegard's law is valid for the β-phase. An empirical correlation between the Nb content and lattice spacing of the β-phase established by Benites et al. [20] is used to calculate the Nb content from the β-phase peak position in the present work. As a result, it was found that the determined Nb content in the β-phase remained virtually in the same range of 76–78% for the all six tubes investigated. These values are higher than the Nb contents in the β-phase of the standard pressure tubes ranging from 32% to 67% [19,21–23] depending on measuring methods and materials.

Fig. 3(b) shows X-ray diffraction patterns of the as-received and the annealed tubes. The second phases in the as-received tubes have completely transformed to β-Nb upon heating at 580 °C for 100 h. The Nb contents in the β-Nb phase of the annealed tubes were in the range of 92–94%, which were determined from the peak positions of (1 1 0) and (2 0 0) reflections of the β-phase. These values are comparable to those of the annealed standard tubes, ranging from 85% to 94% upon 500 °C aging [19,23].

3.2. Tube microstructures

Secondary electron image of the SEM was used to examine substrate microstructures before oxidation. Fig. 4 shows SEM micrographs of various substrates viewed in the radial/axial plane of the tube. The tube microstructure varied significantly with the billet cooling condition only in the case when the tube was extruded at the low temperature of 650 °C. The β-quenched tube (Fig. 4(a)) has a very fine microstructure, having elongated but discontinuous α-Zr (dark area) and β-Zr (light area) phases. Largely different microstructure is observed in the slow-cooled tube (Fig. 4(b)) which has a very coarse α-grains surrounded by filaments of the β-Zr phase.

No significant effect of the billet cooling condition was seen for the tubes extruded at higher temperatures of 815 and 975 °C. These tubes, however, had an inhomogeneous microstructure across the thickness of the tube. For example, in the tubes extruded at 815 °C, the β-phase morphology in the inside of the tube (Fig. 4(c)) is a thin and dense β layer, while a large prior-β area consisting of the mixture of discrete β-Zr and transformed α-phase is observed in the outer side of the tube (Fig. 4(d)). The through-wall variation of the tube microstructure was much more evident for the tubes extruded at 975 °C. The inner side of the tube (Fig. 4(e)) has a coarse Widmanstättan basketweave structure as opposed to a fine discontinuous structure at the outer side of the tube (Fig. 4(f)).

Annealing at 580 °C has changed the α-Zr grain structure and also transformed the second phases (ω- and β-enriched) to β-Nb particles, as illustrated in Fig. 5. The grains of the α-phase were fully re-crystallized, and have a diameter of about 2 μm. The elongated β-Zr filaments of the as-received structure have transformed and discrete particles of about 0.2 μm diameter have precipitated at grain boundaries as well as in the matrix. According to the XRD analysis (Fig. 3(b)), these precipitates represent the β-Nb phase.

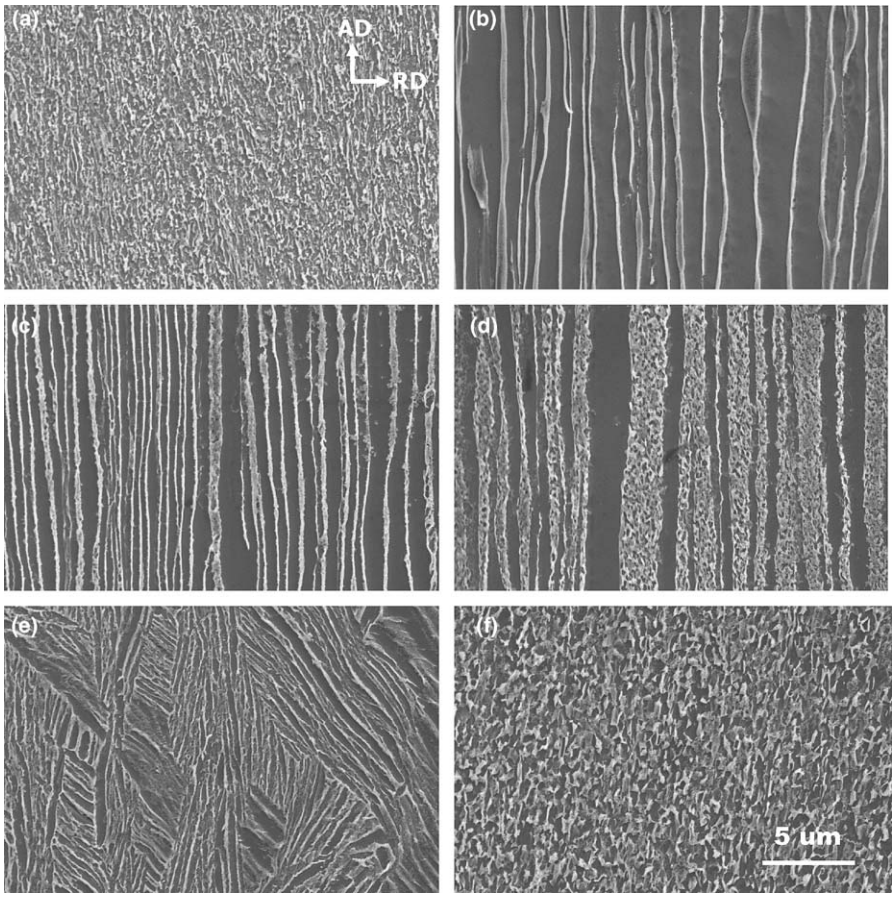

Fig. 4. SEM micrographs of longitudinal/radial planes of the as-received tubes: (a) tube 62, (b) tube 65, (c) inner area of tube 66, (d) outer area of tube 66, (e) inner area of tube 64, and (f) outer area of tube 64.

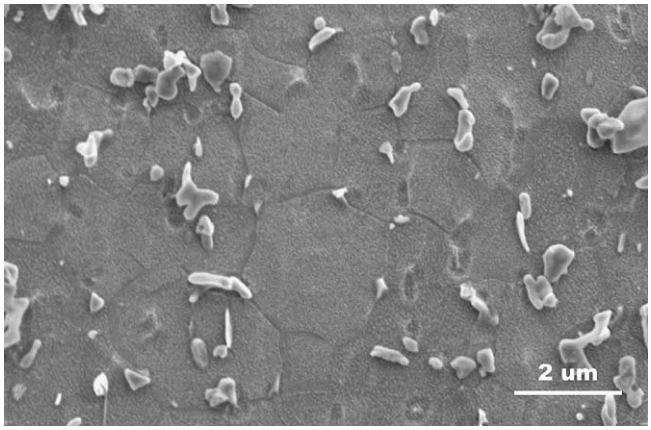

Fig. 5. SEM micrograph of the heat-treated tube 63 at 580 °C for 100 h.

3.3. Oxidation kinetics

Fig. 6 illustrates the TGA test results conducted at 500 °C for the as-received and annealed tubes. Both of the tubes exhibit nearly parabolic oxidation rate since the slopes of the log(*weight gain*) vs. log(*time*) give the values around 0.5. After the heat treatment at 580 °C, the weight gain of the annealed

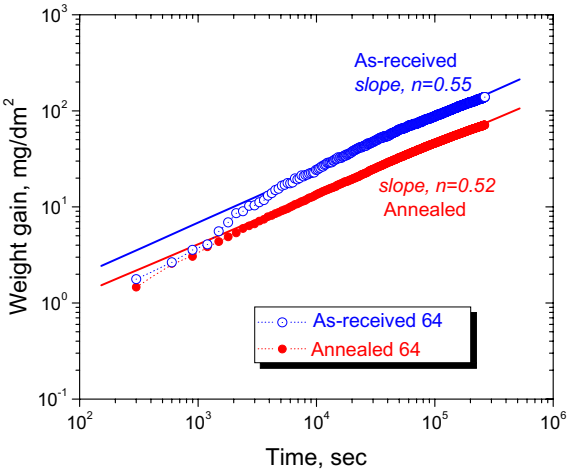

Fig. 6. TGA oxidation results in flowing air at 500 °C.

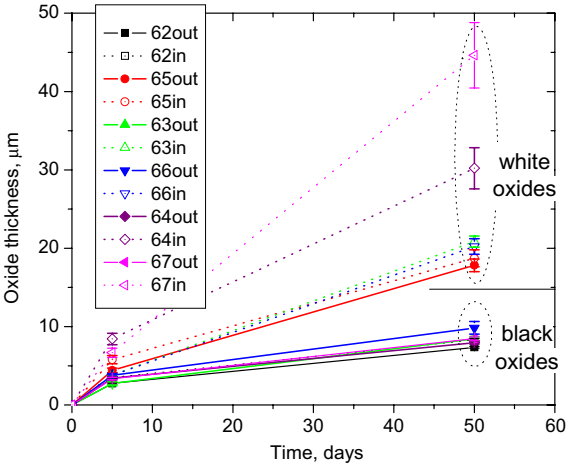

Fig. 8. Oxidation behavior of experimental Zr–2.5Nb tubes in air at 400 °C. The oxide thickness was measured both at outside and inside of the tube.

tube at the end of test decreased by a factor of 2 compared to the as-received one. After the oxidation at 500 °C for three days, it was observed that the β-Zr phase decomposed partly in the as-received tube. This phase decomposition during oxidation test might have an effect on the oxidation kinetics.

To reduce effects of second phase transformations during oxidation test including the β-phase decomposition, the low temperature test was conducted in a furnace at 400 °C. Fig. 7 shows the appearance of tubes after 50 days of exposure. Some tubes exhibit different oxide colors at surfaces between inside and outside of the tube. The oxide color is often considered as an indication of oxidation resistance of Zr alloys. It is well known that black oxides are protective whereas white oxides are non-protective. The measured oxide thickness is shown in Fig. 8, and the higher oxidation rate of the white oxides is evident. The arbitrary line drawn at 15 μm of the oxide thickness in Fig. 8 is a marker that divides the white and black oxides after the 50 days oxidation. The average thickness of the white oxides has a large standard deviation, indicating a localized non-uniform oxidation rate.

3.4. Structures of the oxide–metal interfaces

Fig. 9 shows the morphologies of the oxide–metal interfaces in as-received tubes, which had been oxidized in steam at 400 °C for one day. At this short oxidation time, the oxide interface topography mirrors the substrate structure no matter

Fig. 7. Photographs of the experimental tubes after air oxidation at 400 °C for 50 days.

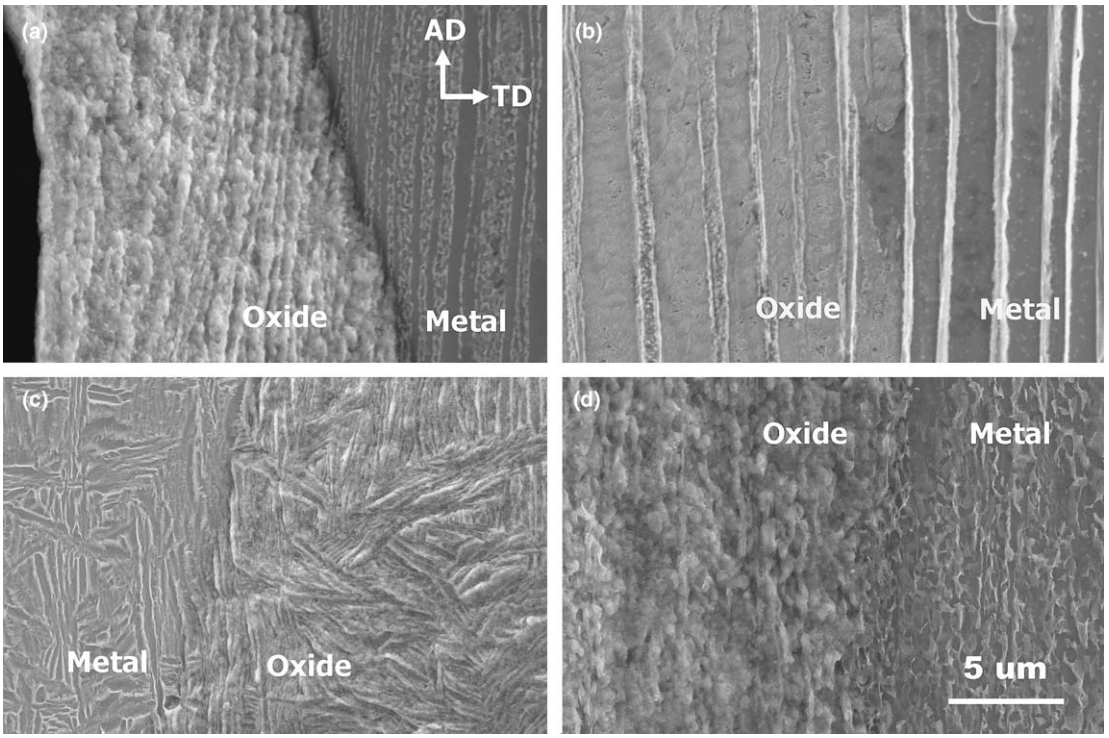

Fig. 9. The oxide–metal interface structures in the as-received tubes (a) outside of tube 63, (b) tube 65, (c) inside of tube 64, and (d) outside of tube 64.

what the metal structure is, forming oxide ridges at the oxide grown on the β-Zr phase. The formation of the oxide ridges indicates a higher oxidation rate at the β-Zr phase regions. The morphology of metal microstructure emerges by the difference of chemical removal rates when the metal is subjected to chemical etching. Since the chemical removal rate of the α-Zr is faster, the β-Zr protrudes from the matrix after etching. These topographic similarities between oxide front and Zr–2.5Nb metal are the reason why these interface structures look alike in SEMs. Fig. 10 shows the oxide interface structures after subsequent oxidation for five days. The oxide ridges formed on the β-Zr were not seen all the area of the oxide interface, and even these were not as apparent as the ridges formed in the thin oxides of the as-received tubes.

After a long oxidation period (50 days), the oxide ridges were hardly seen in the oxide interfaces. As shown in Fig. 11(a), no similarity can be seen between the substrate and the oxide structures at the interface in this long oxidation time. It is interesting to note that the oxide interface structure of the white oxides is quite different from that of the

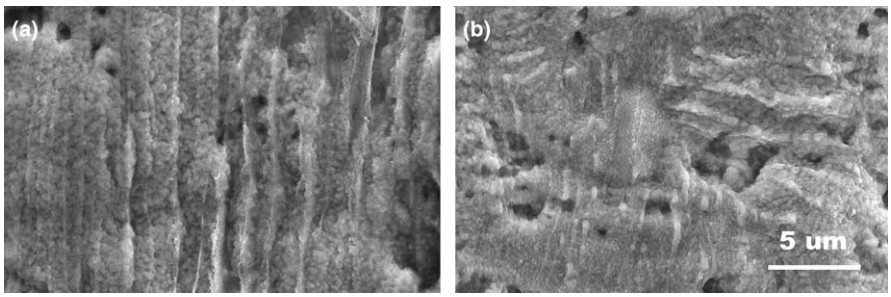

Fig. 10. Oxide interface structures after five days oxidation in 400 °C air (a) tube 65, (b) inside of tube 67.

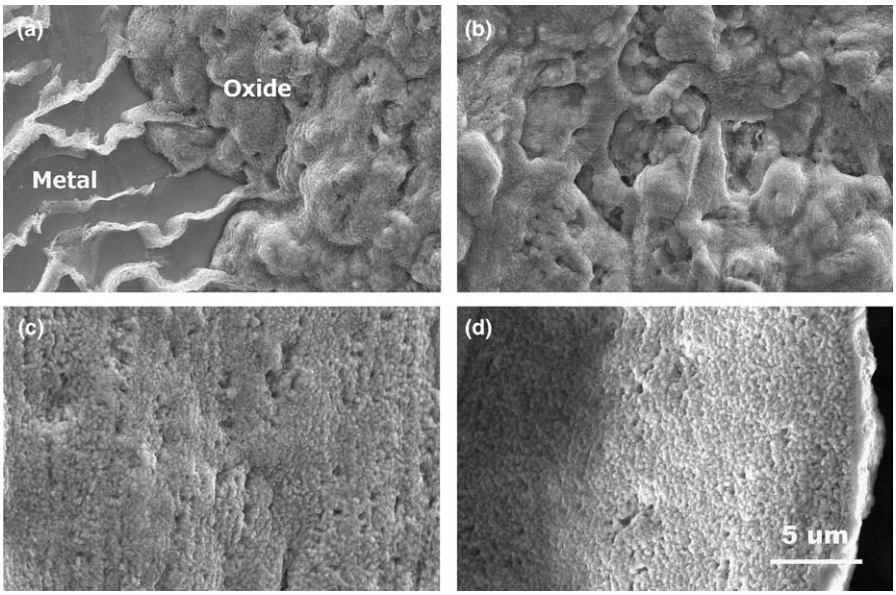

Fig. 11. Oxide interface structures after 50 days oxidation in 400 °C air (a) tube 65, (b) inside of tube 67, (c) outside of tube 66, and (d) outside of tube 67.

black oxides. The white oxides (Fig. 11(a) and (b)) have a highly bumpy and rough interface structure as opposed to a flat and uniform interface structure of the black oxides (Fig. 11(c) and (d)). The rough interface structure of the white oxides was already observed after five days oxidation when the oxide color was still black, and it remained nearly unchanged even after 50 days of oxidation. The rough interface of the white oxides has deep protrusions into the substrate and the oxide protrusion contains small granules inside. In the flat interface of the black oxides, the protrusions are not commonly observed, but instead, the grainy structures of the oxide interface dominate.

Fig. 12 shows the oxide granules developed at various oxidation conditions. Evolution of the granules was observed only in the flat structure of the oxide–metal interface. The small granules start to appear at the interface in the early stage of oxidation (Fig. 12(a)). Their average diameter tends to grow considerably as the oxidation proceeds (Fig. 12(b) and (c)). Moreover, as the oxidation temperature increases from 400 to 500 °C, the granule size becomes even larger although the oxide formed at 500 °C (Fig. 12(d)) is thinner than that formed at 400 °C (Fig. 12(c)). However, there is no such relationship of the granule growth found in the rough interface structure (Fig. 12(e)). The granule diameter is plotted in Fig. 13 as a function of oxide thickness, which clearly shows that the evolution of granule size is significantly different with the morphology of the oxide–metal interface.

4. Discussion

4.1. Tube microstructure and oxidation resistance

The oxidation resistance of zirconium alloys varies with substrate microstructure that is developed as a result of the fabrication process. In Zr–Nb alloys, several metallurgical factors have been suggested in controlling the oxidation resistance: equilibrium Nb content in α-Zr matrix [24], volume fraction of β-Zr phase [19], β-Zr alignment with oxide layer [25], and Nb content in β-Zr phase [13,19]. The effect of equilibrium Nb content in α-Zr on the oxidation resistance is the most prominent only in the case of quenched Zr–Nb alloy that has martensitic α′-Zr. Lin and DeLuca [25] measured Nb contents in α-Zr of Zr–2.5Nb tubes after heating these up to 500 °C and reported that there was not substantial change in the Nb contents. The tubes used in the present experiment were not quenched in the final stage but stress-relieved at 400 °C; therefore, the effect of Nb content in the α-Zr might be insignificant. As for the volume fraction of β-Zr phase, there are controversial results; Urbanic and Griffith [19] demonstrated that corrosion increases with increasing volume fraction of β-Zr while others [25,26] reported that the corro-

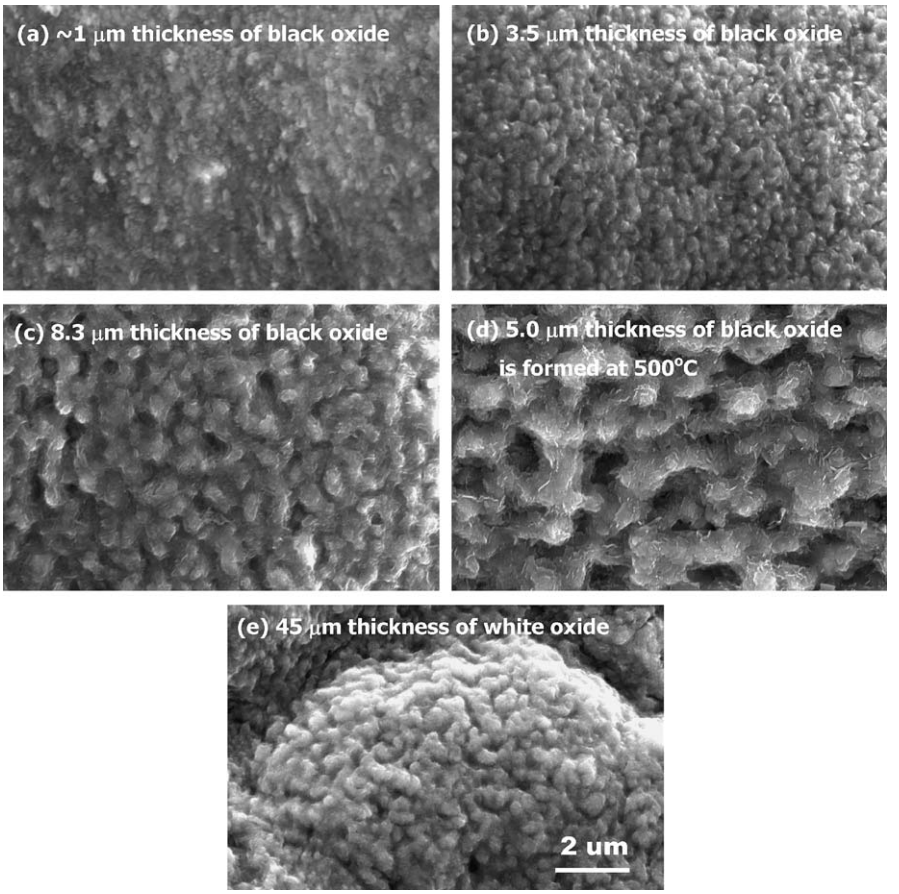

Fig. 12. Oxide granules in (a) as-received tube 62 (autoclaved at 400 °C for one day), (b) oxidized tube 62 at 400 °C for five days, (c) oxidized tube 62 at 400 °C for 50 days, (d) oxidized tube 63 at 500 °C for three days, and (e) oxidized tube 67 at 400 °C for 50 days (inner surface).

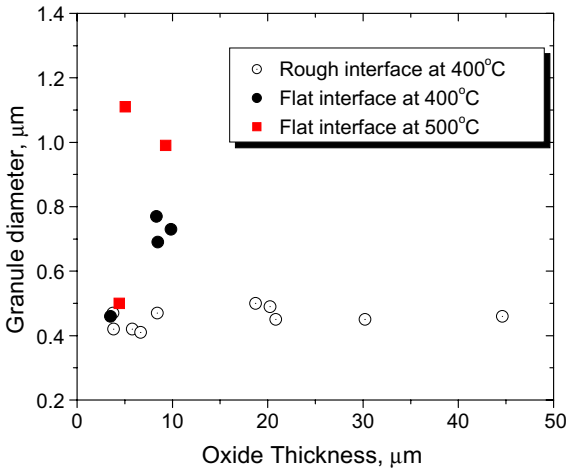

Fig. 13. Variations of the size of oxide granules at the oxide–metal interface as a function of oxide thickness and oxidation temperature.

sion rate does not depend on the amount of β-Zr phase. Lin and DeLuca [25] raised the importance of β-Zr alignment in controlling corrosion rate but they concluded that the decomposition of β-Zr by heat treatment is more significant than the β-Zr alignment. It is generally known that the corrosion resistance increases with the decomposition of β-Zr, which accompanies Nb enrichment in the β-Zr phase. The effect of the β-Zr decomposition on oxidation kinetics is clearly seen in Fig. 6, where the weight gain decreased drastically as the Nb concentration of β-Zr phases increased from 76–78% for the as-received tubes to 92–94% for the annealed tubes.

However, none of the above mentioned factors can explain clearly the significantly different oxidation rates between inner and outer surfaces of the tube (see Fig. 8). There observed the remarkable through-wall variations of the substrate microstructure (see Fig. 4) especially when the tubes were

extruded at higher temperatures. During the tube extrusion process, there probably existed unevenness in terms of deformation and temperature of the tube. Cheadle et al. [27] showed that the region of greatest metal flow during the extrusion process was along the face of the die, that is, on the outer surface of the tube. In addition, the temperature across the tube thickness might not be uniform either. There was significant chilling of the billet during extrusion from the outer surface of the tube because the extrusion chamber was preheated to only 500 °C, which was lower than the extrusion temperatures. The presence of Widmanstättan basketweave structure at inner side of the tube extruded at 975 °C is an indication that the grains developed on cooling after extrusion [9]. On the other hand, the deformed structure of the outer side of the tube indicates that the structure was formed before and/or during extrusion at a temperature that was lower than that of the inner side. These non-uniformities in the processing might lead to through-wall variations in metallographic structures, and this in turn influenced the oxidation rate.

The second phase morphology of the Zr–2.5Nb tubes has an effect on the oxidation resistance. The tubes, which showed lower oxidation rates, for example, tube 62 and outside surfaces of tubes 64 and 67, had the second phases that are fine and discrete structures. In contrast, the tubes of higher oxidation rates (tube 65 and insides of tubes 64 and 67) had coarse and continuous structures of second phases. The through-wall microstructural variation of the tubes extruded at 815 °C (tubes 63 and 66) is not as significant as the tubes extruded at 975 °C, but that is clearer when the tube is looked down the axis of the tube as shown in Fig. 14. The prior-β region at the outer area of the tube consists of α-Zr and discrete second phases while the inner area has a continuous second phase structure. Therefore, it can be concluded that fine dispersion of second phases would help increasing the oxidation resistance of the Zr–2.5Nb tubes significantly.

4.2. Evolution of the oxide–metal interfaces

There may be a close correlation between the interface structure and oxidation rate. As described before, the tube where the interface is formed with the white oxide showed a higher oxidation rate than the tube with the black oxide. The interface with the white oxide has a rough structure. The reason for the formation of the rough interface structure is not clear. But a higher corrosion rate of the rough interface structure is evident elsewhere, for instance, in a single crystal Zr which was corroded at 360 °C water [28]. Local variations in geometry of the interface structure may cause local stress concentrations. A modeling effort on the Zr oxide–metal system showed that cracking appears more likely when the interface is undulated rather than flat [29]. Therefore, zirconium oxides that have a rough interface structure may have more chances of oxide cracking, accelerating the oxidation rate. A larger oxidation area associated with rougher interface structure may also contribute to increasing oxidation rate. The rough interface structure can be, therefore, associated with a higher corrosion rate.

Very little is known about the link between oxide granules in the interface and oxidation rate. At the oxide interface in Zircaloy [1] and Zr [2], it is typical to find structures of fine granules in the pre-transition region and cauliflower-like granules in the post-transition region. The generation of the granular structure is believed to relieve the compressive stress that is concentrated at the oxide interface [4]. The flat oxide interface layer can endure a compressive stress for a longer time because it is more protective than the rough interface structure. Obviously more cracks can be generated at the rough oxide interface and this may hamper the growth of the oxide granules. The

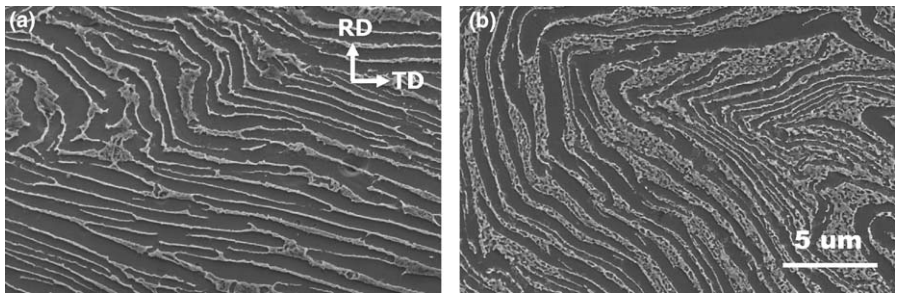

Fig. 14. SEM micrographs of transverse-radial plane of the as-received tube 66: (a) inner side and (b) outer side.

prolonged stability of the flat interface layer may allow the granules to grow to a bigger size.

Higher oxide plasticity at higher temperatures may play a role for making the large oxide granules. It was reported that considerable plasticity occurred in the zirconium oxide at 500 °C [30]. According to Kohli [31], increasing oxidation temperature increased the transition weight gain because the oxide became more plastic as the temperature increased. Such increased plasticity might allow appreciable stress relief in the oxide interface layer. Therefore, at higher temperatures the oxide interface layer deforms easily to relieve a compressive stress. This facilitates the formation of large granules at the oxide interface.

5. Conclusions

Extrusion temperature has a significant impact on the microstructure of Zr–2.5Nb tubes. The tubes that were extruded at $(\alpha + \beta)$ temperature range such as 650 and 815 °C have shown the elongated α-grains surrounded by second phase grain boundaries. The tubes extruded at a β-phase temperature (975 °C) show a Widmanstättan structure at the inner side and a fine discrete structure at outer side of the tube. Billet cooling condition has a relatively little effect on the tube microstructure except the tubes that were extruded at 650 °C, in which the β-quenched tube has very fine grains compared to coarse and elongated grains of the slow-cooled counterpart.

When the tubes were annealed at 580 °C and oxidized at 500 °C, the oxidation weight gain reduced by a factor of 2, but the oxidation kinetics remained parabolic. It is found that the tubes having fine and discrete second phase structures show a superior oxidation resistance to those of coarse and continuous second phase structures including the Widmanstättan structure. The different oxidation rate between the inside and outside surfaces of the tubes is probably due to non-uniformities in temperature and deformation across the tube thickness during the extrusion process.

The evolution of the oxide–metal interface structure was examined by SEM. In the beginning of the oxidation process, the interface structure imitates exactly the substrate structure by forming oxide ridges on β-Zr phases. Then the ridges disappear gradually as the oxide grows. A rough interface structure is formed with higher oxidation rate while a flat and grainy structure develops with a lower oxidation rate. The oxide granule in the flat interface grows more likely in size with increases in oxide thickness and oxidation temperature, but the size of granules is held constant in the rough interfaces. These features of the interface structure may be related to the oxidation resistance.

References

[1] G. Wikmark, P. Rudling, B. Lehtinen, B. Hutchinson, A. Oscarsson, E. Ahlberg, ASTM STP 1295 (1996) 55.
[2] H.S. Hong, S.J. Kim, K.S. Lee, J. Nucl. Mater. 273 (1999) 177.
[3] M. Oskarsson, E. Alhberg, K. Pettersson, J. Nucl. Mater. 298 (2001) 291.
[4] Y. Ding, D.O. Northwood, Corros. Sci. 36 (1994) 259.
[5] A.J.G. Maroto, R. Bordoni, M. Villegas, A.M. Olmedo, M.A. Blesa, A. Iglesias, P. Koenig, J. Nucl. Mater. 229 (1996) 79.
[6] B.D. Warr, E.M. Rasile, A.M. Brennenstuhl, in: Proc. IAEA Technical Committee Meeting on Fundamental Aspects of Corrosion of Zirconium-base Alloys, Portland, USA, 1989, p. 124.
[7] Y. Ding, D.O. Northwood, J. Mater. Sci. 27 (1992) 1045.
[8] R.A. Holt, S.A. Aldridge, J. Nucl. Mater. 135 (1985) 246.
[9] R.A. Holt, P. Zhao, J. Nucl. Mater. 335 (2004) 520.
[10] R. Choubey, S.A. Aldridge, J.R. Theaker, C.D. Cann, C.E. Coleman, ASTM STP 1295 (1996) 657.
[11] H. Li, J. Lin, J. Szpunar, in: 9th Int. Conf. CANDU Fuel, Belleville, Canada, 2005.
[12] O.T. Woo, Y.P. Lin, J. Nucl. Mater. 270 (1999) 376.
[13] V.F. Urbanic, P.K. Chan, D. Khatamian, O.T. Woo, ASTM STP 1245 (1994) 116.
[14] L.W. Hobbs, V.B. Rosen, S.P. Mangin, M. Treska, Int. J. Appl. Ceram. Technol. 2 (3) (2005) 221.
[15] R.C. Asher, D. Davies, T.B.A. Kirstein, J. Nucl. Mater. 49 (1973/1974) 189.
[16] M. Suzuki, S. Kawasaki, J. Nucl. Mater. 140 (1986) 32.
[17] M.G. Glavicic, PhD thesis, McGill University, 1998.
[18] J. Lin, PhD thesis, McGill University, 2005.
[19] V.F. Urbanic, M. Griffiths, ASTM STP 1354 (2000) 641.
[20] G.M. Benites, A.F. Guillermet, G.J. Cuello, J. Campo, J. Alloys Compd. 299 (2000) 183.
[21] A. Perovic, V. Perovic, G.G. Weatherly, G.R. Purdy, R.G. Fleck, J. Nucl. Mater. 199 (1993) 102.
[22] Y.S. Kim, S.S. Kim, Y.M. Cheong, K.S. Im, J. Nucl. Mater. 317 (2003) 117.
[23] D. Khatamian, J. Alloys Compd. 356–357 (2003) 22.
[24] H.H. Klepfer, J. Nucl. Mater. 9 (1963) 65.
[25] Y.-P. Lin, J. DeLuca, J. Nucl. Mater. 265 (1999) 1.
[26] K.N. Choo, Y.H. Kang, S.I. Pyun, V.F. Urbanic, J. Nucl. Mater. 209 (1994) 226.
[27] B.A. Cheadle, S.A. Aldridge, C.E. Ells, Canad. Metallurg. Quart. 11 (1972) 121.
[28] H.G. Kim, T.H. Kim, Y.H. Jeong, J. Nucl. Mater. 306 (2002) 44.
[29] M. Parise, O. Sicardy, G. Cailletaud, J. Nucl. Mater. 256 (1998) 35.
[30] D.L. Douglass, Corros. Sci. 5 (1965) 255.
[31] R. Kohli, J. Nucl. Mater. 91 (1980) 85.